MESOSCOPIC PHYSICS

Electron collision in a two-path graphene interferometer

H. Chakraborti[1]†, L. Pugliese[1]†, A. Assouline[1]‡, K. Watanabe[2], T. Taniguchi[2], N. Kumada[3], D. C. Glattli[1], M. Jo[1]§, H.-S. Sim[4]*, P. Roulleau[1]*

The collision of two electrons at a beam splitter provides a method for studying their coherence and indistinguishability. Its realization requires the on-demand generation and synchronization of single electrons. In this work, we demonstrate the coherent collision of single electrons, generated by voltage pulses, in a graphene Mach-Zehnder interferometer. By measuring shot noise resulting from the collisions, we unveil fundamental characteristics of colliding electrons, highlighting the complementarity between the indistinguishable and distinguishable parts of their wave functions. The former is manifested through fermionic Hong-Ou-Mandel destructive interference, whereas the latter is discerned through double-winding Aharonov-Bohm interference in the noise. The interference visibilities of around 60% enable comprehensive quantum state tomography. Our findings may place coherent operations involving flying qubits within reach in graphene.

Coherent manipulation of single particles enables us to explore their wave nature and exploit it for quantum information processing. In particular, the scattering of single particles at beam splitters is a fundamental building block for generating single-particle or multiparticle interferences (*1*–*3*), providing valuable insights into the quantum statistics of identical particles, such as bosons, fermions, and anyons (*4*–*11*), as well as quantum entanglement among them (*12*). When two indistinguishable electrons collide at a beam splitter, antibunching occurs (*13*, *14*), manifesting as the fermionic analog of the Hong-Ou-Mandel (HOM) effect (*4*). This effect results from the fermionic statistics, where the wave functions of two identical fermions satisfy $\Psi(1,2) = e^{i\theta_s}\Psi(2,1)$ with $\theta_s = \pi$, when the positions of the fermions are exchanged. This collision process can be extended to dynamical generation of orbital entanglement and subsequent detection of its quantum nonlocality (*12*). Furthermore, the collision process is a key element of a quantum state tomography (*15*). In this protocol, a target electron wave packet collides with a small coherent field consisting of electron-hole pairs, and the target state is reconstructed from two-electron interference involving exchange between the target electron and the electron-hole pairs. Demonstrating the collision of two electrons is therefore a milestone in the realization of "flying qubits" for electron quantum optics, where a propagating single-electron wave packet carries information encoded in its orbital degree of freedom. This requires electron sources (*13*, *16*) emitting coherent single-electron wave packets, precise control of the emission energy and timing, manipulation of a beam splitter, and measurement of collision states through shot noise. Additionally, it demands ballistic channels for wave packet propagation that are robust against noise and decoherence. Recently, there have been advancements in electron Mach-Zehnder or Fabry-Perot interferometers in graphene (*17*–*21*). These cutting-edge interferometers showed single-particle Aharonov-Bohm interference persisting even at high electron temperatures of 2 K and voltages of 1 mV, which suggests that graphene is a promising platform for flying qubits.

In this work, we report a two-electron collision in a two-path interferometer. We integrate on-demand manipulation of dynamical electron excitations, an electronic Mach-Zehnder interferometer (MZI), and detection of the fermionic HOM interference in a graphene quantum Hall device. The dynamical electron excitations are generated by applying voltage pulses simultaneously to a pair of electrical contacts, with precise control of the time delay between the pulses. These excitations propagate along quantum Hall edge channels and collide at the MZI. The resulting fluctuations of electrical current or shot noise, measured as a function of the time delay and the magnetic flux enclosed by the MZI, unveil the following fundamental aspects of two-electron collision.

The noise shows the HOM oscillation as a function of the time delay. It exhibits a minimum value at zero time delay, when the two excitations simultaneously reach the MZI. The minimum results from a destructive two-electron interference, a consequence of the fermionic exchange statistics and the indistinguishability between the two colliding excitations; the minimum value is independent of the magnetic flux enclosed by the MZI. By contrast, when the time delay is such that the two excitations are maximally distinguishable, the HOM noise shows a maximum. The maximum value depends on the flux in the MZI and shows $h/2e$ Aharonov-Bohm oscillations, where h is the Planck constant and e is the electron charge. This single-electron interference results from the distinguishable part of the colliding excitations, and the $h/2e$ oscillations indicate "double winding" of an electron around the Aharonov-Bohm flux that happens with the help of an auxiliary hole when the electron is detected in the noise—a two-particle observable. The HOM and $h/2e$ oscillations offer the witness of the full (two-particle and single-particle, respectively) coherence structure of the collision. Finally, we demonstrate the quantum state tomography of a Leviton (a clean electron excitation carrying no extra electron-hole pairs), further underlining the potential of our graphene setup for quantum information processing.

HOM experiment

The sample used is a monolayer graphene quantum Hall pn junction (Fig. 1A). A global graphite gate and a metallic top gate (top G) on the right half of the sample allow us to independently tune the filling factors on the left and right halves. In the n (left half) and p (right half) regions, the filling factors are set to $\upsilon_N = 2$ and $\upsilon_P = -2$, respectively. As a result, in each of the p and n regions, two channels flow along the top physical edge of the graphene sample from a source contact toward the pn interface; another pair of channels flows along the bottom edge from the pn interface toward a drain contact. Along the pn interface, four channels copropagate. Two side gates, SG_1 and SG_2, positioned at the top and bottom intersections between the pn interface and the physical edges, respectively, serve as (top and bottom) beam splitters (*18*). Tuning the filling factors υ_1 and υ_2 underneath the gates controls the transmission and reflection of the channels between the p and n sides. When $\upsilon_1 = 2$ and $\upsilon_2 = 0$, only the top beam splitter operates, allowing an electron moving along the top edge of the n (p) region to be transmitted to the p-side (n-side) channel of the pn interface with probability T_1; no transmission happens between the n and p sides at the bottom intersection. Conversely, when $\upsilon_1 = 0$ and $\upsilon_2 = 2$, only the bottom beam splitter operates with a transmission probability T_2. The electron spin is preserved in the beam splitting (*17*, *18*). When $\upsilon_1 = \upsilon_2 = 2$, both beam splitters partially transmit, leading to the formation of a MZI (*18*, *19*).

[1]SPEC, CEA, CNRS, Université Paris-Saclay, CEA Saclay, Gif sur Yvette Cedex, France. [2]National Institute for Materials Science, 1-1 Namiki, Tsukuba, Japan. [3]NTT Basic Research Laboratories, NTT Corporation, 3-1 Morinosato-Wakamiya, Atsugi, Japan. [4]Department of Physics, Korea Advanced Institute of Science and Technology, Daejeon, South Korea. ***Corresponding author. Email: hssim@kaist.ac.kr (H.-S.S.); preden.roulleau@cea.fr (P.R.)** †These authors contributed equally to this work. ‡Present address: CNRS, Institut Néel, Grenoble, France. §Present address: Department of Physics, Kyungpook National University, Daegu, South Korea.

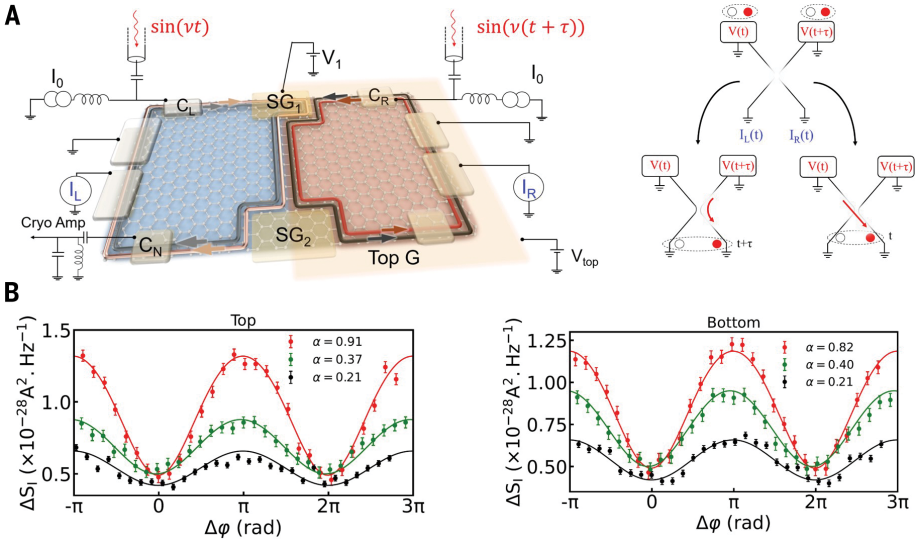

Fig. 1. HOM experiment in the single beam splitter configuration. (**A**) (Left) Schematic representation of the sample in the bipolar regime ($\upsilon_N = 2$, $\upsilon_P = -2$) set by the global back and right top gates. The filling factors below the upper and lower side gates (SG_1 and SG_2) are set to $\upsilon_1 = 2$ and $\upsilon_2 = 0$, respectively. Two sine pulses with a time delay τ collide on the top beam splitter. (Right) Indistinguishability of colliding excitations. In the top panel, electron-hole pairs are emitted from the left and right sources with a time delay τ. In the bottom left (right) panel, the pair from the right (left) source is split at the beam splitter into a hole moving to the left drain and an electron to the right drain. When $\tau = 0$ (i.e., $\Delta\varphi = 0$), the two pairs are fully indistinguishable because they arrive at the beam splitter at the same time. Then, the scattering events in the bottom left and right panels cannot happen simultaneously because of a destructive two-particle interference (Pauli exclusion). When the delay is the largest ($\Delta\varphi = \pi$), the two pairs are the most distinguishable because their wave function overlap at the beam splitter is the smallest. The events in the two bottom panels occur independently, involving the distinguishable parts of the wave functions. (**B**) Shot noise as a function of the delay time ($\Delta\varphi$) when electron-hole pairs collide at either the top beam splitter (left) or bottom beam splitter (right), for frequencies of 5 (in red), 9 (in green), and 15 GHz (in black). The experimental results (filled dots) agree with theoretical curves (solid lines) (*24*).

We first consider $\upsilon_1 = 2$ and $\upsilon_2 = 0$, where only the top beam splitter operates. We apply sinusoidal voltage pulses $V_L(t) = V_{ac}\cos(2\pi\nu t)$ and $V_R(t) = V_{ac}\cos(2\pi\nu t + \Delta\varphi)$ to the left (C_L) and right (C_R) contacts, respectively, with the relative phase $\Delta\varphi = 2\pi\nu\tau$, where ν represents the excitation frequency and τ denotes time delay between the two pulses. The resulting photo-created electron-hole pairs flow from each contact to the pn interface. They undergo collision and partitioning at the top beam splitter, generating autocorrelation shot noise $S_I = 2\int dt\left\langle \delta I_N(t+t_0)\delta I_N(t_0)\right\rangle$ of the electrical currents I_N measured at a drain contact C_N. Here, $\delta I_N(t) \equiv I_N(t) - \left\langle I_N(t_0)\right\rangle$ is the current fluctuation and $\langle\cdots\rangle$ denotes an average over time t_0. The left panel of Fig. 1B shows the shot noise at frequencies of $\nu = 5$, 9, and 15 GHz for different photon numbers $\alpha = eV_{ac}/h\nu$ at 20 mK. It oscillates with the relative phase $\Delta\varphi$. As expected, similar oscillations are observed at $\upsilon_1 = 0$ and $\upsilon_2 = 2$, where only the bottom beam splitter operates so that the photo-created electron-hole pairs collide and then are partitioned at the bottom beam splitter (Fig. 1B, right). The oscillatory behavior results from the two-particle fermionic HOM interference. It agrees with the theoretical expression of the HOM noise at finite temperature (*22*, *23*)

$$S_I^{HOM} = S_I^0 F(\Delta\varphi), F(\Delta\varphi) = \sum_{l=-\infty}^{+\infty}\left[l\coth\left(\frac{l}{2\theta_e}\right) - 2\theta_e\right]J_l^2\left[2\alpha\sin\left(\frac{\Delta\varphi}{2}\right)\right] \quad (1)$$

The factor $S_I^0 = 2\frac{2e^2}{h}D(1-D)h\nu$ represents the characteristic scale of the photo-assisted shot noise, where the factor 2 accounts for the two channels at each physical edge of the p and n regions, and $D = T_1$ for $\upsilon_1 = 2$ and $\upsilon_2 = 0$, whereas $D = T_2$ for $\upsilon_1 = 0$ and $\upsilon_2 = 2$. $\theta_e = k_B T_e/h\nu$, where T_e is the temperature and k_B is the Boltzmann constant, l is the number of absorbed or emitted photons, and J_l is the Bessel function.

The oscillation of the noise S_I^{HOM} as a function of $\Delta\varphi$ exhibits its minimum value (the HOM dip) when the time delay τ is zero (i.e., $\Delta\varphi = 0$). This results from the destructive two-electron interference by the indistinguishability of the two colliding excitations. At $\Delta\varphi = 0$, the two excitations, one generated by $V_L(t)$ at the left source C_L and the other by $V_R(t)$ at the right source C_R, arrive at the beam splitter at the same time so that they are fully indistinguishable in their collision (Fig. 1A, right). They cannot occupy the same outgoing state after the collision owing to the Pauli exclusion principle. As a result, their antibunching always occurs (namely, one of them moves to the n side after the collision, whereas the other moves to the p side), resulting in no noise. By contrast, the noise reaches its maximum value (the HOM peak) when $\Delta\varphi = \pi$. In this case, the two excitations are the most distinguishable because their wave functions have the smallest overlap in the collision. The distinguishable parts of the wave functions are free from Pauli exclusion, and they undergo single-particle scattering at the beam splitter, which is probabilistic and hence generates noise. At intermediate $\Delta\varphi$, the two excitations are partly indistinguishable, resulting in an intermediate value of the noise. Therefore, the dependence of the noise on $\Delta\varphi$ serves as a witness of the two-particle coherence of the collision. In Fig. 2B, we observe that the noise S_I^{HOM} does not drop to zero. This offset of S_I^{HOM} (~5.10^{-29} A^2/Hz) is attributed to heating by the ac signal, which generates thermal noise [further details are available in the supplementary materials (*24*)]. We note that when only $V_L(t)$ is applied [i.e., $V_R(t)$ is turned off], the noise follows the photo-assisted shot noise formula, which is identical to Eq. 1 except for the replacement of the last factor $J_l^2\left[2\alpha\sin\left(\frac{\Delta\varphi}{2}\right)\right]$ with $J_l^2(\alpha)$ (*25*).

HOM effect in the MZI

We next consider the MZI formed at $\upsilon_1 = 2$ and $\upsilon_2 = 2$, where both the top and bottom beam splitters operate (*17*, *18*). The channels along the top and bottom physical edges in the p and n regions serve as the input and output channels of the MZI, respectively, whereas the n-side and p-side channels running along the pn interface constitute the two MZI arms. At the top beam splitter, the n-side (p-side) input channels are scattered into the p-side (n-side) MZI arm with the transmission probability T_1 and into the n-side (p-side) MZI arm with the reflection probability $R_1 = 1 - T_1$. Inside the MZI, there is no scattering between the arms. At the bottom beam splitter, the interface channels are scattered into the output channels with the transmission T_2 and reflection $R_2 = 1 - T_2$ probabilities similarly to the top beam splitter. The two beam splitters and the two arms enclose a magnetic flux that induces the Aharonov-Bohm phase φ_{AB}. Figure 2A shows the h/e Aharonov-Bohm oscillation of the transmission through the MZI for $T_1 \approx T_2 \approx 0.5$, obtained by standard low-frequency lock-in measurement.

Next, we study the HOM effects in the MZI by applying the sinusoidal voltage pulses to the sources C_L and C_R while measuring the shot noise at the drain C_N. To observe the HOM effect, conditioned by the indistinguishability of the input states, the powers applied to the

sources must be precisely equal. To ensure this condition, we tuned the powers individually and measured the Aharonov-Bohm oscillation of the excess shot noise (defined as the shot noise difference with and without the sinusoidal voltage pulses) by applying the sine pulse voltage to either C_L (Fig. 2B) or C_R (Fig. 2C) (*25*). By comparing the measured oscillation with theory (*24*, *26*), we confirmed that the voltages applied to the two sources have the same amplitude. Next, the sine voltage pulses are applied to both sources with the relative phase $\Delta\varphi$, and the resulting Aharonov-Bohm oscillations of the shot noise are measured. At $\Delta\varphi = 0$, the noise exhibits its minimum value (HOM dip), as in Fig. 1B. In this case, no Aharonov-Bohm oscillation is observed (Fig. 2D). By contrast, at $\Delta\varphi = \pi$, the noise has the maximum value (HOM peak) and exhibits $h/2e$ Aharonov-Bohm oscillations.

These observations agree with our theory for the MZI (*24*)

$$S_I^{\text{HOM-MZI}} = S_I^{0,\text{MZI}} F(\Delta\varphi), S_I^{0,\text{MZI}} = 2\frac{2e^2}{h} T_{\text{MZI}}(1-T_{\text{MZI}})h\nu$$

where $T_{\text{MZI}} = R_1T_2 + T_1R_2 + 2\sqrt{R_1T_1R_2T_2}\cos\varphi_{\text{AB}}$ is the transmission probability through the MZI. This equation is valid when the MZI arms have equal length (*18*, *19*) and the two sources have the same value of $\alpha = eV_{\text{ac}}/h\nu$, as in our case. It has the same form as Eq. 1 but with replacement of the photo-assisted shot noise scale S_I^0 by $S_I^{0,\text{MZI}}$. Equation 2 shows that the noise vanishes at $\Delta\varphi = 0$, $F(\Delta\varphi = 0) = 0$ and that no Aharonov-Bohm oscillation happens at $\Delta\varphi = 0$. By contrast, at $\Delta\varphi \neq 0$, the colliding particles are partly distinguishable, resulting in the $h/2e$ Aharonov-Bohm oscillation of the noise, which is described by $T_{\text{MZI}}(1-T_{\text{MZI}}) = (1-\cos 2\varphi_{\text{AB}})/8$ at $T_1 = T_2 = 0.5$. We observed that the $h/2e$ Aharonov-Bohm oscillation is more visible when the colliding particles are more distinguishable with $\Delta\varphi$ closer to π, whereas the destructive two-particle interference of the fermionic HOM effect becomes stronger when the particles are more indistinguishable with $\Delta\varphi$ closer to 0. This represents the complementarity between the two-particle HOM interference and the single-particle $h/2e$ Aharonov-Bohm interference. This complementarity is maximally evident in our MZI with equal arm lengths, where the indistinguishability of the colliding particles at the top beam splitter remains unchanged at the bottom beam splitter. This fermionic complementarity can be compared with other fundamental complementarities (*27*–*29*), such as those between single-particle and two-particle interferences.

We describe a simple picture for the findings. We consider a case of $\Delta\varphi = 0$, where two electrons—one injected from C_L and the other from C_R—simultaneously arrive at the MZI, or a case of $\Delta\varphi = \pi$, where only the electron from C_L arrives at the MZI (the other from C_R is ignored because it does not arrive at the MZI). In these cases where C_L emits an electron $\left[\text{i.e.,}\left\langle c_L^\dagger c_L\right\rangle = 1\right]$, the noise $S_I^{\text{HOM-MZI}} \propto \left\langle c_N^\dagger c_N c_N^\dagger c_N\right\rangle - \left\langle c_N^\dagger c_N\right\rangle^2$ at C_N is expressed as

$$S_I^{\text{HOM-MZI}} \propto \left\langle t^* c_L^\dagger r c_R r^* c_R^\dagger t c_L\right\rangle = T_{\text{MZI}}(1-T_{\text{MZI}})\left\langle c_L^\dagger c_L\right\rangle\left\langle c_R c_R^\dagger\right\rangle \quad (3)$$

Here, $c_{L/R/N}^\dagger$ is the operator creating an electron in a state of $C_{L/R/N}$ and obeys $c_N = tc_L + rc_R$, with the scattering amplitudes t and r in the MZI satisfying $|t|^2 = T_{\text{MZI}}$ and $|r|^2 = 1 - T_{\text{MZI}}$. Equation 3 shows that the noise vanishes at $\Delta\varphi = 0$, where $\left\langle c_L^\dagger c_L\right\rangle = 1$ and $\left\langle c_R^\dagger c_R\right\rangle = 1$ $\left[\text{i.e.,}\left\langle c_R c_R^\dagger\right\rangle = 0\right]$. This is caused by the antibunching of the two injected electrons that are fully indistinguishable in the MZI when $\Delta\varphi = 0$. By contrast, the noise exhibits the $h/2e$ Aharonov-Bohm oscillation of $S_I^{\text{HOM-MZI}} \propto T_{\text{MZI}}(1-T_{\text{MZI}}) = (1-\cos 2\varphi_{\text{AB}})/8$ at $\Delta\varphi = \pi$, where $\left\langle c_L^\dagger c_L\right\rangle = 1$ and $\left\langle c_R^\dagger c_R\right\rangle = 0$ $\left[\text{i.e.,}\left\langle c_R c_R^\dagger\right\rangle = 1\right]$. The term $\cos 2\varphi_{\text{AB}}$ results

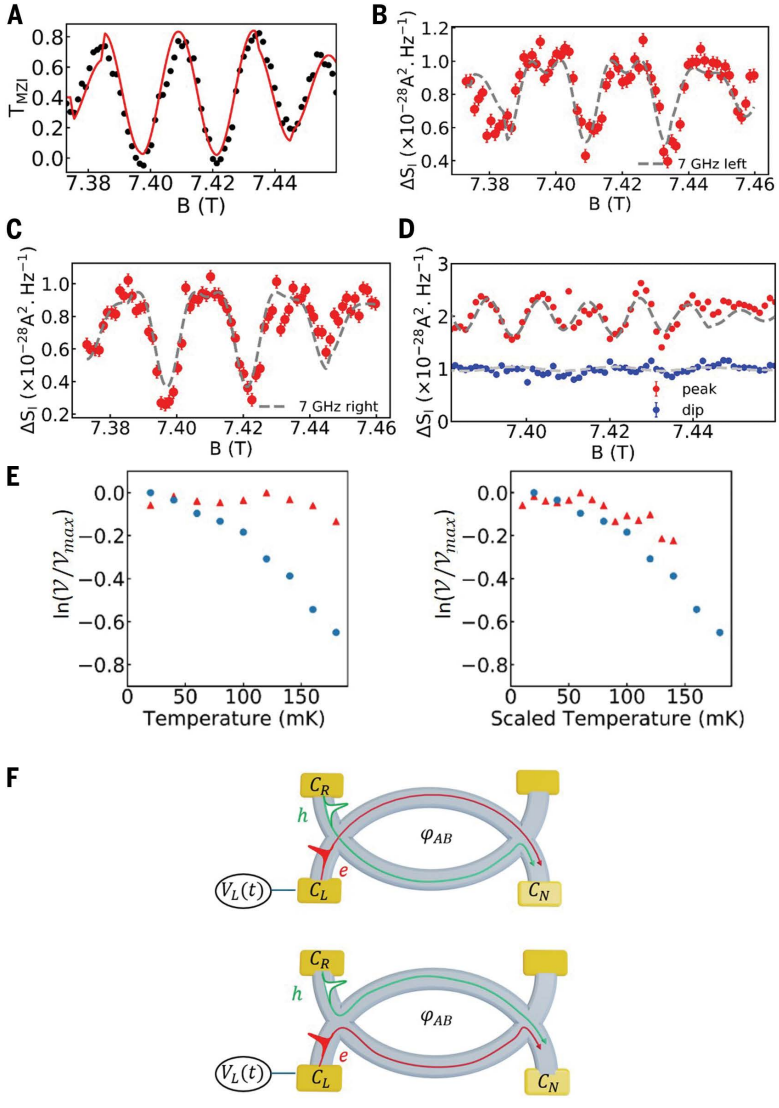

Fig. 2. Noise in the Mach-Zehnder configuration. (**A**) Transmission (T_{MZI}) of the MZI (dots) as a function of the magnetic field. The solid curve shows the theoretical result (*24*). (**B** and **C**) Excess shot noise $S_I^{\text{HOM-MZI}}$ (red dots) as a function of the magnetic field for the 7-GHz sine pulse excitation applied on either the left source (B) or the right source (C). The dashed curves show the theoretical fits (*24*). (**D**) The excess shot noise $S_I^{\text{HOM-MZI}}$ as a function of the magnetic field for the sine pulse applied on both sources with $\Delta\varphi = 0$ (blue dots; HOM dip) and $\Delta\varphi = \pi$ (red dots; HOM peak). The offset noise for $\Delta\varphi = 0$ is caused by the thermal noise (*24*). The dashed curves are the theoretical fits (*24*). (**E**) (Left) Aharonov-Bohm interference visibilities $\mathcal{V}$ of the measured transmission T_{MZI} (red triangles) and the noise $S_I^{\text{HOM-MZI}}$ (blue dots) as a function of temperature T. The decrease of the visibility with temperature is more pronounced for the interference of $S_I^{\text{HOM-MZI}}$. $\mathcal{V}_{\text{max}}$ is the maximum value of the visibility. (Right) The decay of the interference visibility of the noise $S_I^{\text{HOM-MZI}}$ is redrawn with the scaled temperature $T_s = 2T$, whereas that of the transmission T_{MZI} is drawn with $T_s = T$. The two decay curves become nearly identical, which suggests that the interference length scale is two times as large for the noise. (**F**) Schematic illustration of the double winding, which results from an interference between process (i) (bottom) and process (ii) (top). The injected electron (depicted by the red full peak) and the auxiliary hole (the green empty peak) follow the red and green trajectories, respectively.

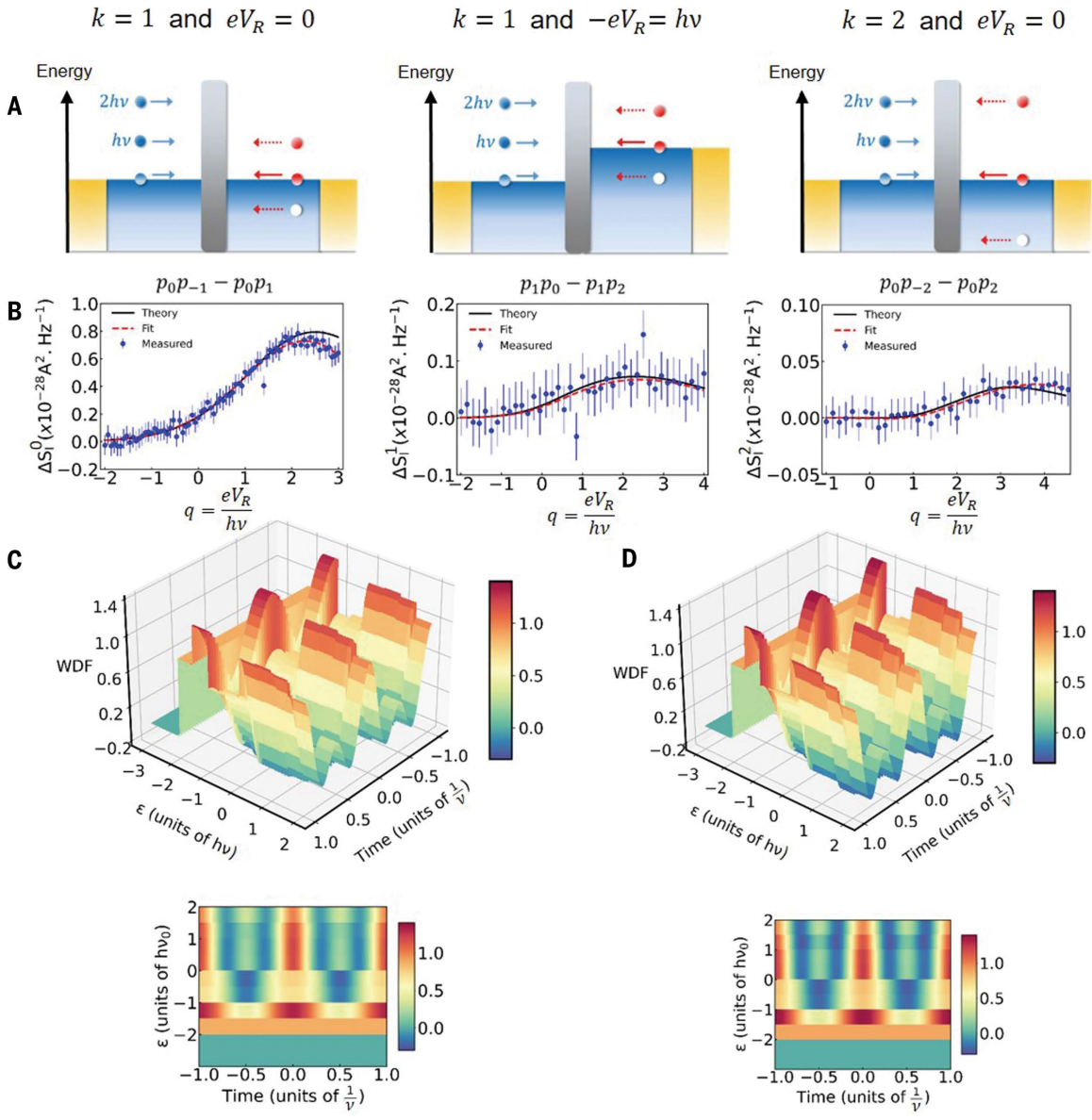

Fig. 3. Tomography of the 2*e* Leviton. (**A**) Schematic representation of the tomography protocol: Lorentzian pulses are applied at frequency ν on the left ohmic contact to generate Levitons in the Fermi sea (shown in blue). For the tomography protocol, the Lorentzian pulse is engineered with three harmonics (*26*). The Levitons are described by a coherent superposition of plane waves (blue dots) of energy $hm\nu$ (with $m = 0, 1, 2, \cdots$) induced by the Lorentzian pulses. A small ac local oscillator is applied at frequency $k\nu$ on the right contact to generate an ac voltage $V_{LO}(t) = \eta_{LO}\left(\frac{h\nu}{e}\right)\cos\left[2\pi k\nu(t-\tau)\right]$ superimposed to a dc voltage V_R. The resulting fermion field is a superposition of plane waves of energy $-eV_R$, $-eV_R \pm hk\nu$ describing electron-hole pairs (red and empty dots). The Levitons and the fermion field collide at a beam splitter (vertical gray bar). (Left) $k = 1$ and $V_R = 0$. In this configuration, cross terms $p_0p_{-1} - p_0p_1$ are computed. (Middle) $k = 1$ and $-eV_R = h\nu$ for computing of $p_1p_0 - p_1p_2$. (Right) $k = 2$ and $V_R = 0$ for computing of $p_0p_{-2} - p_0p_2$ (*24*). (**B**) $\Delta S_i^{k=0}$ with $V_R = 0$ (left), $\Delta S_i^{k=1}$ with $-eV_R = h\nu$ (middle), and $\Delta S_i^{k=2}$ with $V_R = 0$ (right) as a function of $q = eV_R / h\nu$. The measurement allows for the computation of the energy density matrix. (**C**) Reconstructed Wigner distribution function (WDF) from the tomography measurement. The two-dimensional color plots are shown to better display the region of negative values of the Wigner distribution function. (**D**) Theoretical Wigner distribution function in the energy/time basis (*24*).

from the interference between processes (i) and (ii) (Fig. 2F). In (i), the electron injected from C_L moves along the left arm of the MZI, and an auxiliary (or virtual) hole, describing the condition of $\left\langle c_R^{\dagger} c_R \right\rangle = 0$ that the electron state injected from C_R is unoccupied, moves along the right arm of the MZI. This process is equivalent with an "anticlockwise" winding of an electron around the Aharonov-Bohm flux enclosed by the MZI and gains the phase factor of $e^{i\varphi_{AB}}$. In (ii), the electron moves along the right arm, whereas the auxiliary hole moves along the left arm. This gains the phase factor of $e^{-i\varphi_{AB}}$ by a clockwise winding of an electron around the flux. The interference between (i) and (ii) involves the net phase factor of $e^{2i\varphi_{AB}}$ by a double winding of an electron around the flux. The double winding effectively happens in the noise with the help of an auxiliary hole because the noise is a two-particle observable. It differs from the multiple winding in a Fabry-Perot interferometer or a quantum ring (*20*, *21*).

We next analyze the single-particle coherence of the collision. The $h/2e$ Aharonov-Bohm oscillation at $\Delta\varphi = \pi$ in Fig. 2D can be fitted with Eq. 2 using $\alpha = eV_{ac} / h\nu$. In the left panel of Fig. 2E, the visibility of the $h/2e$ Aharonov-Bohm oscillation—defined as $\mathcal{V} = S_{max} - S_{min}$ with the maximum (S_{max}) and minimum (S_{min}) values of the noise—is shown as a function of temperature T_e from 20 mK to 300 mK and compared with the visibility of the h/e Aharonov-Bohm oscillation of T_{MZI} extracted from

the data in Fig. 2A. The temperature dependences of the two visibilities are well aligned if the temperature for the noise visibility is scaled up by a factor of 2 (Fig. 2E, right). The factor 2 reflects the fact that the noise is associated with the double winding around the magnetic flux as described above, involving twice the MZI arm length ($S_I^{\text{HOM-MZI}} \sim e^{-2L/L_\varphi}$, with L the arm length and L_φ the single-particle coherence length); the interference involving the double winding experiences twice as much decoherence as the single winding. Such scaling is explained by a decoherence model based on intrachannel Coulomb interactions (*19*). In this model, the single-particle visibility follows a universal curve with scaled temperature LT/L_0 by the MZI arm length L (L_0 is a reference length). In graphene, the Coulomb interaction between the colliding electrons and several decoherence sources such as interchannel interactions are suppressed owing to the close proximity of metallic gates, which screen the interactions and freeze decoherence below ~350 mK for the arm length of 1.5 μm (*19*). The suppression is crucial for manipulating the collision states and observing the complementarity.

Quantum state tomography of a Leviton

The excellent coherence observed in our setup underscores its potential for quantum information processing. A natural application of the collision is the full reconstruction of a quantum state or quantum state tomography (*15*, *30*). We perform the tomography of a Leviton (*13*) with charge $2e$ at $\upsilon_1 = 2$ and $\upsilon_2 = 0$ (where only the top beam splitter is operated). The overall process unfolds as follows: A series of the Levitons are injected from C_L by applying Lorentzian voltage pulses $V(t)$ with frequency ν. Simultaneously, a low-intensity fermionic field, which is a coherent superposition of electron-hole pairs, is injected from C_R by applying a small ac voltage $V_{LO}(t) = \eta_{LO}\left(\frac{h\nu}{e}\right)\cos\left[2\pi k\nu(t-\tau)\right]$ superimposed to a dc voltage V_R with amplitude $\eta_{LO} \ll 1$, frequency $k\nu$ (an integer multiple of the Leviton frequency ν), and time delay τ referred to the Leviton emission time. The Levitons and the fermionic field collide at the beam splitter, generating antibunching effects. By measuring the resulting shot noise, the Wigner distribution function $W(t,\varepsilon) = \int_{-\infty}^{\infty} d\delta\rho(\varepsilon+\delta/2, \varepsilon-\delta/2)e^{-i\delta t/\hbar}$ of the Leviton is reconstructed.

We next provide the details of the tomography (*15*). The energy density matrix $\rho(\varepsilon,\varepsilon')$ of the Leviton is expressed as $\rho(\varepsilon,\varepsilon'\neq\varepsilon) = \sum_k \delta(\varepsilon'-\varepsilon-kh\nu)\tilde{\varphi}^*(\varepsilon+kh\nu)\tilde{\varphi}(\varepsilon)$ for the periodic injection of the Levitons, where δ is the Dirac delta function, $\tilde{\varphi}(\varepsilon)$ is the Fourier transform of the Leviton wave function $\varphi\left(t-\frac{x}{v_F}\right)$ at position x and time t, and v_F is the velocity. The wave function product $\rho_{l,l+k} \equiv \tilde{\varphi}^*(\varepsilon+kh\nu)\tilde{\varphi}(\varepsilon)$ for the energy domain $lh\nu < \varepsilon < (l+1)h\nu$ is written as $\rho_{l,l+k} = -\sum_{m=-n}^{l} p_m p_{m+k}$ for the Leviton of charge ne (in our case, $n = 2$) (*24*). Here, p_m is the amplitude of the Leviton wave function component generated by absorption ($m > 0$) or emission ($m < 0$) of m photons thanks to the Lorentzian voltage $V(t)$. It equals the Fourier coefficient of the phase factor by the voltage, $\exp\left[-i\frac{e}{\hbar}\int_o^t V(t')dt'\right] = \sum_m p_m e^{-i2\pi m\nu t}$. To obtain $p_m p_{m+k}$, we measured the noise difference ΔS_I^k between the cases with the ac voltage $V_{LO}(t)$ turned on and off. The extraction of $p_m p_{m+k}$ from the noise uses the theoretical expression (*24*) of $\frac{\Delta S_I^{k\neq 0}}{S_I^0} = \eta_{LO}\cos(2\pi k\nu\tau)\sum_m |m-q|\left(p_m p_{m-k} - p_m p_{m+k}\right)$, with $q = eV_R/h\nu$ for $k \neq 0$. This describes collision between the plane waves of energy $mh\nu$ (with $m = 0, 1, 2, \cdots$) forming the Levitons and the plane waves of energy $-eV_R$, $-eV_R \pm hk\nu$ forming the fermion field (Fig. 3A), which is the underlying mechanism of the tomography. By changing q for k = 0,1,2, we extract relevant $p_m p_{m+k}$ (Fig. 3B), compute $\rho_{l,l+k}$ using them, and reconstruct the Wigner distribution function (Fig. 3C). The result agrees with the theoretical prediction (Fig. 3D). Through the implementation of this method, we gain a deeper understanding compared with the conventional HOM measurement that only yields the wave function overlap between the colliding electrons.

Discussion and outlook

Our work opens a door to coherent operations of flying qubits for entanglement (*12*) and two-particle quantum state tomography (*31*). Moreover, these reference experiments can be extended to anyonic excitations, enabling on-demand manipulation (*22*), measurement of anyonic statistical phases (*32*), and braiding operations.

REFERENCES AND NOTES

1. Y. Ji *et al.*, *Nature* **422**, 415–418 (2003).
2. P. Roulleau *et al.*, *Phys. Rev. B* **76**, 161309 (2007).
3. I. Neder *et al.*, *Nature* **448**, 333–337 (2007).
4. C. K. Hong, Z. Y. Ou, L. Mandel, *Phys. Rev. Lett.* **59**, 2044–2046 (1987).
5. M. Henny *et al.*, *Science* **284**, 296–298 (1999).
6. W. D. Oliver, J. Kim, R. C. Liu, Y. Yamamoto, *Science* **284**, 299–301 (1999).
7. R. C. Liu, B. Odom, Y. Yamamoto, S. Tarucha, *Nature* **391**, 263–265 (1998).
8. H. Bartolomei *et al.*, *Science* **368**, 173–177 (2020).
9. J.-Y. M. Lee *et al.*, *Nature* **617**, 277–281 (2023).
10. P. Glidic *et al.*, *Phys. Rev. X* **13**, 011030 (2023).
11. M. Ruelle *et al.*, *Phys. Rev. X* **13**, 011031 (2023).
12. P. Samuelsson, M. Buttiker, *Phys. Rev. B* **71**, 245317 (2005).
13. J. Dubois *et al.*, *Nature* **502**, 659–663 (2013).
14. E. Bocquillon *et al.*, *Science* **339**, 1054–1057 (2013).
15. T. Jullien *et al.*, *Nature* **514**, 603–607 (2014).
16. G. Fève *et al.*, *Science* **316**, 1169–1172 (2007).
17. D. S. Wei *et al.*, *Sci. Adv.* **3**, e1700600 (2017).
18. M. Jo *et al.*, *Phys. Rev. Lett.* **126**, 146803 (2021).
19. M. Jo *et al.*, *Nat. Commun.* **13**, 5473 (2022).
20. C. Déprez *et al.*, *Nat. Nanotechnol.* **16**, 555–562 (2021).
21. Y. Ronen *et al.*, *Nat. Nanotechnol.* **16**, 563–569 (2021).
22. I. Taktak *et al.*, *Nat. Commun.* **13**, 5863 (2022).
23. V. S. Rychkov, M. L. Polianski, M. Buttiker, *Phys. Rev. B* **72**, 155326 (2005).
24. See the supplementary materials.
25. A. Assouline *et al.*, *Science* **382**, 1260–1264 (2023).
26. P. P. Hofer, C. Flindt, *Phys. Rev. B* **90**, 235416 (2014).
27. G. Jaeger, A. Shimony, L. Vaidman, *Phys. Rev. A* **51**, 54–67 (1995).
28. D. Kaszlikowski, L. C. Kwek, M. Zukowski, B.-G. Englert, *Phys. Rev. Lett.* **91**, 037901 (2003).
29. P. Busch, C. Shilladay, *Phys. Rep.* **435**, 1–31 (2006).
30. C. Grenier *et al.*, *New J. Phys.* **13**, 093007 (2011).
31. P. Samuelsson, M. Büttiker, *Phys. Rev. B* **73**, 041305 (2006).
32. J.-Y. M. Lee, C. Han, H.-S. Sim, *Phys. Rev. Lett.* **125**, 196802 (2020).
33. P. Roulleau, Electron Collision in a Two-Path Graphene Interferometer, data set, Zenodo (2025).

ACKNOWLEDGMENTS

We thank F. Parmentier for his help in fabrication, L. Bernabeu and S. Lee for discussion in the early stage of the work, and M. Kuiri for his help on the manuscript. **Funding:** This work was funded by the ERC starting grant COHEGRAPH 679531 (P.R.), by the EMPIR project SEQUOIA 17FUN04 cofinanced by the participating states and the European Union's Horizon 2020 program (P.R.), by ANR EQUBITFLY (P.R.), by Horizon-EIC-2022-Pathfinderopen project FLATS (P.R.), and by Korea NRF through the SRC Center for Quantum Coherence in Condensed Matter (grant no. RS-2023-00207732) (H.-S.S.). **Author contributions:** H.C., L.P., A.A., and P.R. performed the experiment. H.C., L.P., A.A., N.K., D.C.G., H.-S.S., and P.R. analyzed and discussed the data. T.T. and K.W. provided the boron nitride layers. H.-S.S. and P.R. wrote the manuscript with input from all coauthors. H.-S.S. developed the theory. M.J. fabricated the device with input from A.A. and P.R. P.R. designed and supervised the experiment. **Competing interests:** The authors declare no competing interests. **Data and materials availability:** Data and code are available on Zenodo (*33*).

SUPPLEMENTARY MATERIALS

science.org/doi/10.1126/science.adn4622
Materials and Methods; Supplementary Text; Figs. S1 to S3; Table S1; References (*34*, *35*)
Submitted 11 December 2023; accepted 13 March 2025
10.1126/science.adn4622